Acta Geodaetica et Geophysica (2019) 54:461–481
https://doi.org/10.1007/s40328-019-00276-2

ORIGINAL STUDY

Future stress accumulation zones around the main active faults by 3D numerical simulation in East Azerbaijan Province, Iran

Pouya Sadeghi-Farshbaf[1] · Mohammad Mahdi Khatib[2] · Hamid Nazari[3]

Received: 15 June 2019 / Accepted: 8 November 2019 / Published online: 13 November 2019

Abstract
As a preliminary three-dimensional numerical analysis, this research aims to detect future zones of high-stress accumulation caused by the interaction of active faults within a 3D topographic geological block based on finite-element analysis. Stress analysis of the three-dimensional topographic model covers both static and dynamic loading caused by topographic loads and crustal movements, and can provide more realistic results. There are many applications to create topographic models from *xyz* data. Nevertheless, these models do not have the properties required in analytical software. Solid meshing of topographic blocks is abstruse and consumes much time and high CPU usage. Therefore, we first try to create a validated topographic shell model through the introduced methods including nodal projection and statistical analysis, and then upgrade it to a solid model. The stress equations are then assigned to each element of the solid model. The outputs include stress accumulation zones in both pre-failure and failure mode for the whole model. In addition, energy diagrams show the rate of main energies per time and accordingly, represent the perception of power for each energy output. Energy drop during the initial run time is consistent with the collision of the blocks of the model.

Keywords Solid meshing · Numerical analysis · Stress accumulation · Energy

✉ Pouya Sadeghi-Farshbaf
pouya.sadeghi@birjand.ac.ir

Mohammad Mahdi Khatib
mkhatib@birjand.ac.ir

Hamid Nazari
h.nazari@gsi.ir

[1] Tectonics Laboratory, Department of Geology, Pardis Campus, University of Birjand Blvd, Avini Blvd, Birjand 97174-34765, Iran

[2] Department of Geology, University of Birjand, Birjand, Iran

[3] Research Institute for Earth Sciences, Tehran, Iran

1 Introduction

Stress accumulation in the Earth leads to the development of structures such as faults, folds, and joints. Seismicity can result due to the action of anomalous local stress concentrations or a tectonic stress field acting on preexisting zones of weakness or both (Talwani 1990). The estimation of tectonic stresses is important for structural geologists for studies of geodynamic (Pollard 2000), foundation engineering (Amadei and Stephansson 1997), and subsurface fluid flow (Mandl 2000; Nelson 1985). The stress accumulation model makes specific predictions about the distribution of events in an accelerating moment release (AMR) (Mignan et al. 2006).

Stress trajectory changes due to the interacting geological blocks make zones of stress accumulation. It is therefore, necessary to understand the mechanism of block motion in different directions and to understand the nature of stress accumulation to predict the future respective events in space and time. 3D finite elements (FEs) for the realistic numerical simulation of certain problems of the Earth systems science such as seismicity, fault mechanics, geodynamics, and ground instability are more useful. A main factor of accumulating stress is related to regional tectonic loading (Xiao and He 2015). Another important factor affecting the stress buildup along active faults is after a moment release of an individual earthquake, the state of stress on nearby faults could be redistributed both by co-seismic deformation and by postseismic viscoelastic relaxation of the lower crust and upper mantle (Deng and Sykes 1997; Freed et al. 2007; Pollitz et al. 2004; Ryder et al. 2012). 3D numerical simulations strongly dependent on FE models that consist of a network of elements. Therefore, mesh generation as a process of dividing a continuous physical domain into a grid (elements) for the further numerical solution (Xing et al. 2009) is one of the most important stages of modeling. Since affecting a stress direction and stress field of a study area to one structural feature needs to consider the feature as a solid part (Sadeghi-Farshbaf et al. 2015), each 3D FE model needs to be formed from solid meshes.

Primary studies were carried out about stress accumulation and release on the San Andreas Fault (Turcotte 1977) based on elastic theory. Some studies have considered stress accumulation due to a long dip slip fault movement (Debnath and Sen 2013), stress accumulation rates along the primary segments (Smith and Sandwell 2003), stress concentration using seismic data (Chen et al. 2014), and stress accumulation and seismic risk (Nalbant et al. 2002). Some authors (e.g., Fuis et al. 2012) discussed the geometry of the fault and relationship to lithospheric structure. In most of these works, the media were taken to be elastic and/or viscoelastic, but a layered model with the viscoelastic layer(s) over viscoelastic half space will be a more realistic one for the lithosphere-asthenosphere system (Debnath and Sen 2013). Some modern studies dealt with the role of structural heterogeneities (e.g., Carminati et al. 2001; Carminati and Vadacca 2010), rheological feedback (Dal Zilio et al. 2018), topographical loading (Sadeghi-Farshbaf 2016), and mechanical deformation (Chéry et al. 2004; Sadeghi-Farshbaf 2010; Rhoden et al. 2012; Sadeghi-Farshbaf et al. 2015) in their models. However, the concept of the modern mechanical model is rooted in some of the older studies (e.g. Bombolakis 1989; Niño et al. 1998; Chéry et al. 2001). Applying such thermo-mechanical parameters to three-dimensional models related to stress analysis can provide more realistic results.

Because of the major difficulties associated with the use of three-dimensional elements (Rao 2011), a large number of equations related to the solid model need to be solved. Logically, removing topography will not solve the problem, because without considering topography, the results are far from reality due to loading derived by inverse and direct isostasy

(Abd-Elmotaal 2013; Mareschal and Kuang 1986) and concentration of most stress–strain as well as dynamic analysis of the topography. On the other hand, high CPU usage and misfits as a result of solid meshing of such geometries (Pain et al. 2002) is another modeling problem.

To solve stress equations, both finite difference (FD) and FE methods are required. FE is advantageous at irregular geometry in two and three-dimensional domains (Sadeghi-Farshbaf et al. 2015). Some researchers used unstructured tetrahedral meshes for FEA (e.g., Allik and Hughes 1970; Caendish et al. 1985; Garimella 2002) while others used it in interpolation of samples (Sambridge et al. 1995), shape reconstruction (Boissonnat 1988), and description the topography of the measurement area with high accuracy (Günther and Rücker 2005). However, both tetrahedral or hexahedral meshes are used for numerical analysis of the solid part, we have performed our analysis on the solid topographic model suggested by the authors (Sadeghi-Farshbaf et al. 2015) based on tetrahedron elements.

In this research, we try to perform stress analysis on our previously created standard 3D FE topographic model for East Azerbaijan (EA) (Sadeghi-Farshbaf et al. 2015). For tectonic purposes, the geometry of the fault is required for analysis, and this geometry is added to the block. Finally, by definition the stress shape functions for solid meshes, we create a stress interpolation model for whole volume of the block.

The study area includes important active faults and topographic variations, and therefore, we continue to analyze our previously created topographic model. The process includes positioning the active faults in the solid model, Identifying the faults in the specified nodal network, and stress analysis.

2 Active faults positioning

North Tabriz Fault (NTF), North Bozghush Fault (NBF), Sought Bozghush Fault (SBF), Arasbaran Fault (AF), Ahar Fault (AhF), and Sufian Fault (SF) in EA are selected as important active faults with a history of destructive earthquakes (Vasheghani-Farahani and Zaré 2014). Figure 1 shows the study area and the mentioned faults. The placement of a fault in the model is based on the selection of nodes corresponding to the points located on the fault plane.

3 Faults identifying

To identify the faults to the model, the following steps must be taken beforehand:

- Applying the Quaternary alluvial deposits to the model. The thickness of this layer is about 200–300 m in the study area.
- Applying the sedimentary layer to the model. According to Teknik and Ghods (2017), an average thickness of this layer has been considered about 5 km in the study area.
- Applying the seismogenic layer to the model. According to Herrin et al. (2002), earthquakes larger than 5 have been selected due to SNR signals for teleseismic earthquakes, and therefore the depth criterion of 55 km (about 11.5 km for each element) has been considered.

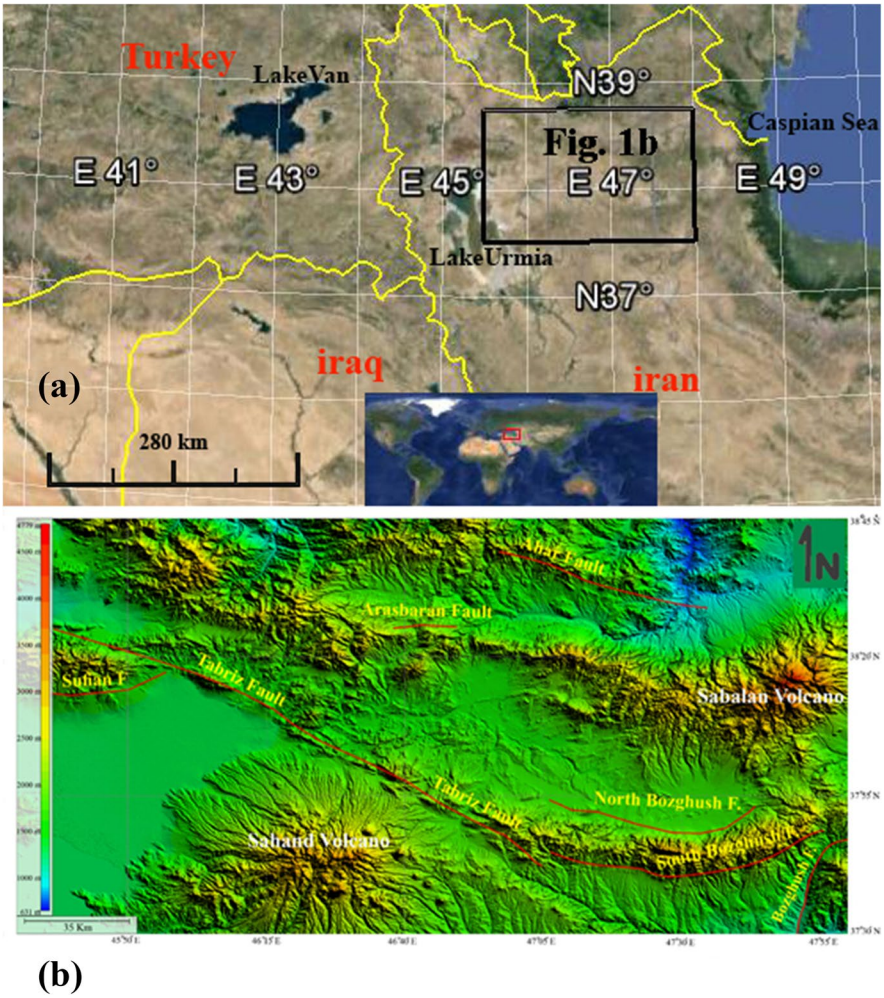

Fig. 1 Location of the study area. **a** Regional Google Earth image showing the position of the study area (black inset). **b** GTOPO30. Shaded relief image of the study area in East Azerbaijan including active faults and important volcanoes

4 Meshing

The mesh sizes of the original shell model have been calculated by using the statistical measurements related to topographic variables and cut surface areas (CSAs). The solid model has been meshed by definition of shape functions for the whole model volume. Due to the importance of the role of topography in the analysis phase of this study, the mesh sizes have been based on statistical calculations of the topographic surface. Selecting a rectangular region as a default type of region-selection on the digital elevation map (DEM) is the first stage (Fig. 1b).

It has been an effort to keep main heights and active faults as an analytic meshed part. Considering the effect of topographic variations in mesh sizes will be possible by getting CSAs

to the sections covering the main heights and active faults. Since CSA calculations require a datum level, we select a contour line with the biggest perimeter as a datum level in the second stage. In this case, the contour line of 1700 m is regarded as datum level (Figs. 2, 3).

The third stage is creating some sections from the main heights with the same intervals. CSAs related to the seven sections covering the main heights and active faults have been calculated to obtain required statistical parameters for the study area (Table 1).

The area of the projected topographic surface onto a horizontal plane is simply equal to product of length and width,

$$A = LW \tag{1}$$

where L is the length and W is the width of the projected study area. In the study area, this value is 30,360 sq. km. The standard deviation of maximum elevation (Table 1) is useful to consider the effect of topographic variations on the mesh spacing. The standard deviation is written as:

$$\sigma = \sqrt{(1/N-1)\sum_{i=1}^{N}(h_i - \bar{h})^2} \tag{2}$$

where N denotes the number of the highest topographic peaks in all sections and $(h_i - \bar{h})^2$ is squared differences of the height values. To emphasize the importance of the effects of the number of topographic peaks higher than datum plane and determine whether the differences are statistically significant, we use standard error as follows:

$$S_e = \sqrt{[1/N(N-1)]\sum_{i=1}^{N}(h_i - \bar{h})^2} \tag{3}$$

One of the variables to determine the mesh sizes, is the topographic volume. To estimate this variable, calculating the geometric mean as an average of CSAs is required,

$$\mu_{GCSA} = \left(\prod_{i=1}^{M} S_i\right)^{1/M} \tag{4}$$

where M is the number of sections and S is the area of each cut surface. Consequently, the function of average volume of the topographic part of the model can be written as:

$$V = \mu_{GCSA} W \tag{5}$$

The greater the area and the topographic variations, the lower the accuracy of user-computed mesh sizes. The more the area the more general the meshing. In addition, the more scattered the topographic peaks, the smaller the size required for analysis. We use standard error to emphasize the role of the number of the highest topographic peaks in the mesh spacing. Therefore, the maximum mesh spacing is a result of all mentioned statistical measurements:

$$D_{max} = (A\sigma S_e)/V \tag{6}$$

From Eq. (6):

$$D_{max} = L[(1/N-1)\sum_{i=1}^{N}(h_i - \bar{h})^2] \Big/ \left[\left(\prod_{i=1}^{M} s_i\right)^{1/M}\right]\sqrt{N} \tag{7}$$

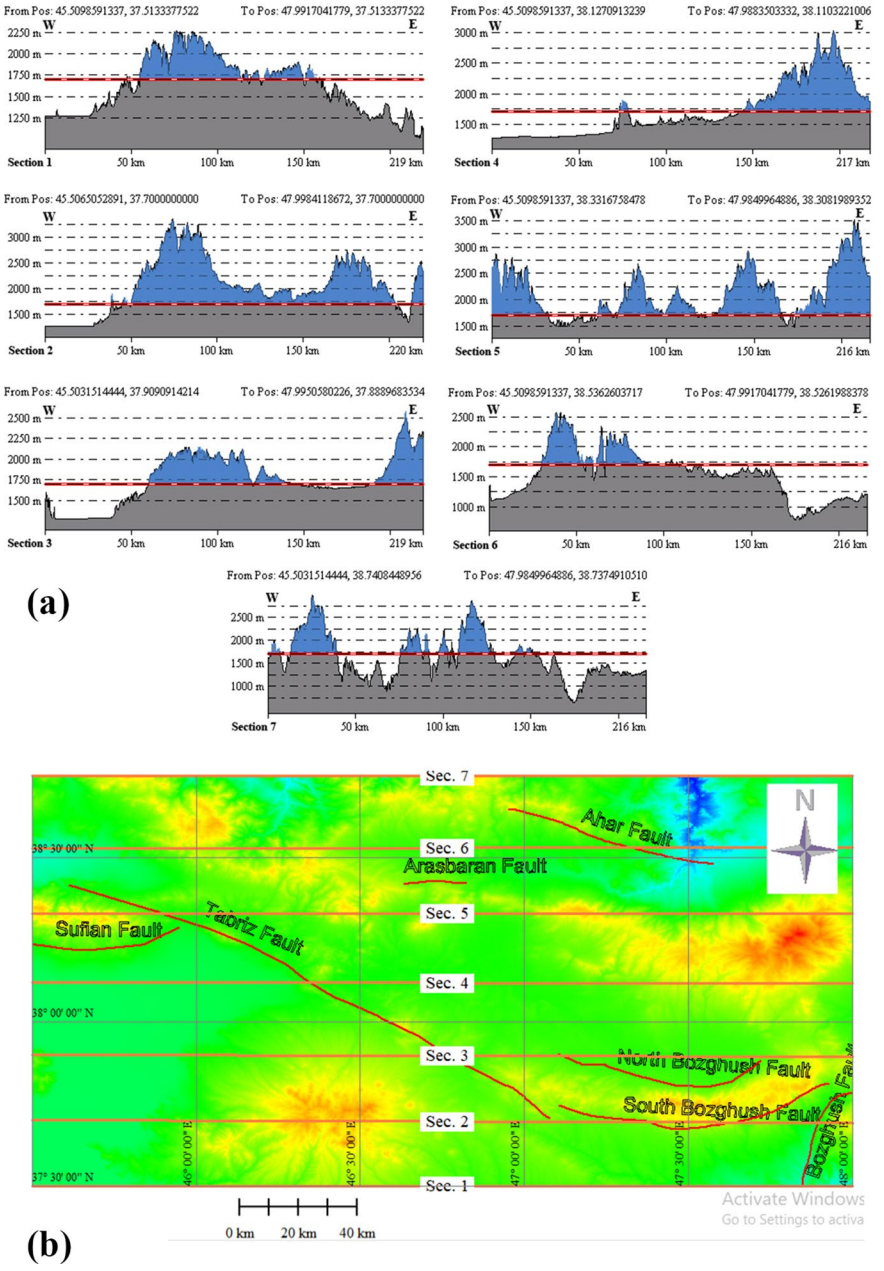

Fig. 2 **a** CSA calculations based on datum level for most topographic heterogeneities in seven sections. **b** The position of the sections in the study area

where D_{max} is the maximum mesh dimension that is used for mesh spacing. Table 2 shows the results of μ_{GCSA}, V, and D_{max}. D_{max} for the study area according to Eq. (7) is 11.5 km. This means that the maximum mesh size usable for the model is 11.5 km.

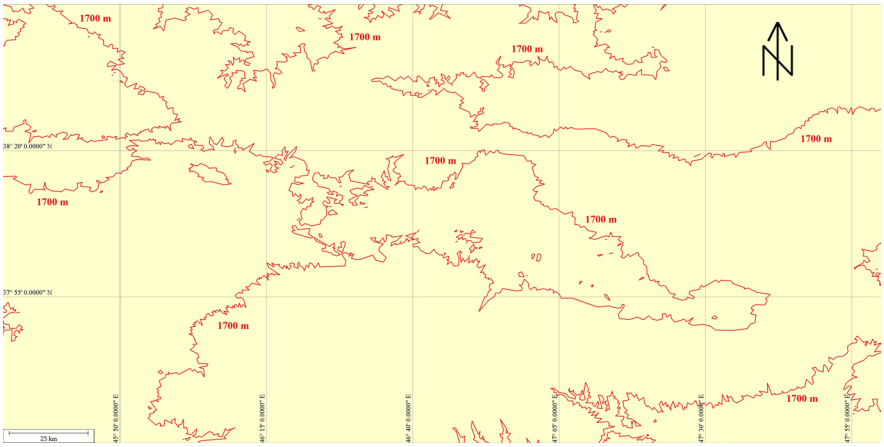

Fig. 3 Datum level in the study area (see text)

Table 1 Statistical data calculated for the seven cross-sections

Section	Cut surface area (km^2)	Maximum elevation (m)	Standard deviation (km)	Standard error (km)	Geometric mean for CSA (km^2)
1	1.301	2250	0.445	0.168	1.354
2	1.634	3300			
3	1.388	2570			
4	1.177	3050			
5	1.632	3500			
6	1.115	2550			
7	1.232	2900			

All elevation data used for CSAs are higher than datum plane

Table 2 Maximum mesh dimension from geometric mean of CSA and statistical measurements (see text)

Parameter	Value (km^2)
Average CSA	1.354
Volume	186.852
D_{max}	11.5

The primitive 3D topographic shell model had been constructed by applying this mesh size to the topographic surface as well as the lines created by the projection of two-dimensional element nodes onto a horizontal plane located at the desired depth (Fig. 4). The depth of projection depends on the purposes of the study. Since most numerical studies on active tectonics and stress distribution are conducted by considering faults and seismicity (e.g. Lysmer and Drake 1972; Pereyra et al. 1992; Bai and Xu 2013; Shao and Hou 2019), the earthquakes distribution pattern has been analyzed in

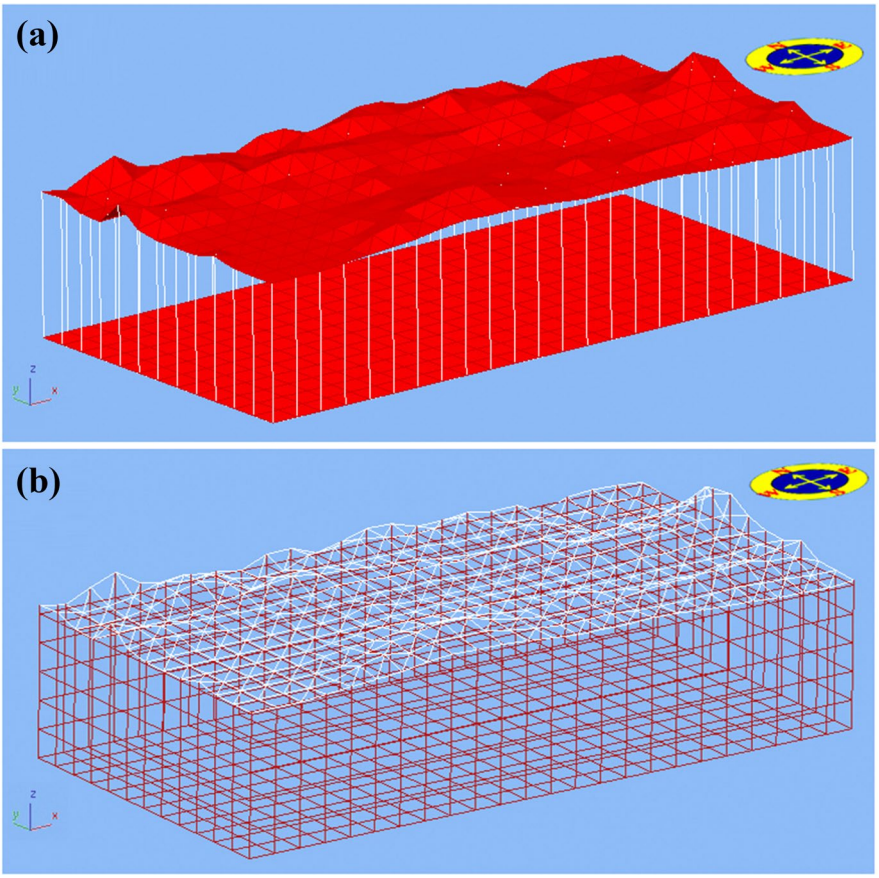

Fig. 4 3D constructed shell model from **a** nodes projecting, and **b** 3D meshed topographic block diagram

Table 3 Earthquake catalogue for East Azerbaijan with a minimum magnitude of five

Date	Latitude	Longitude	Depth (km)	Magnitude	Region
5-8-1930	37.7	45.5	33	Ms:5.1	West of Azarshahr
3-20-1960	38.25	46		M:5.2	East Azerbaijan, East of Shabestar
2-10-1965	37.66	47.09	45	mb:5	East Azerbaijan, North of Hashtrud
8-24-1984	38.5	45.95	10	mb:5.1	East Azerbaijan, East of Marand
3-2-1997	37.99	47.89	15	Mw:5.3	East Azerbaijan, West of Nir
8-11-2012	38.55	46.87	15	Mb:6.1	East Azerbaijan, West of Ahar
8-11-2012	38.58	46.78	16	Mb:6.1	East Azerbaijan, North-West of Ahar
8-14-2012	38.46	46.76	14	ML:5.2	East Azerbaijan, West of Ahar
8-15-2012	38.45	46.66	14	ML:5.1	East Azerbaijan, West of Ahar
11-7-2012	38.48	46.57	14	ML:5.6	East Azerbaijan, West of Ahar

Earthquake data are from IIEES

this study (Table 3). Selecting earthquakes equal or larger than 5 is due to the avoidance of the SNR signals (Herrin et al. 2002).

In terms of clustered and dispersed distribution patterns, we select the deepest hypocenter and mean hypocenters as the study depth, respectively. Average Nearest-Neighbor index (ANN) (Davis 1986) is useful to determine the pattern of spatial distribution. The basis of this index is the measurement of distance between each point data and its nearest neighbor's point data location as follows:

$$ANN = \bar{D}_O / \bar{D}_E \tag{8}$$

where $\bar{D}_O$ is the observed mean distance between each point data and their nearest neighbor:

$$\bar{D}_O = \sum_{i=1}^{n} d_i / n \tag{9}$$

and $\bar{D}_E$ is expected mean distance from the point data given a random pattern:

$$\bar{D}_E = 0.5 / \sqrt{n/A} \tag{10}$$

where d_i equals the distance between point i and its nearest neighbor, n corresponds to the total number of points and, A is the total study area. The ANN index of the hypocenter pattern in the study area is less than 1, denoting a clustered distribution pattern. Therefore, the deepest hypocenter has been selected as the depth of the model, that is, an optimal third dimension.

Due to the possibility of error in the hypocenter depth data (Billings et al. 1994), the third dimension of the model is equal to the maximum depth plus the D_{max},

$$T_d = Hyp_{max} + D_{max} \tag{11}$$

where Hyp_{max} is the maximum depth of the hypocenters. T_d has been calculated as 55 km according to the Eq. (11).

Finally, the 3D topographic solid model has been built by importing and validating the 3D shell model in any analytical software (e.g., ANSYS, ABAQUS, and CATIA), selecting appropriate structured meshes, and meshing the model based on D_{max}.

5 Model properties

In this study, the model had been made of solid meshes and therefore the model parameters had also defined according to the solid components.

Although viscous flow in the deep crust and uppermost mantle can contribute to the accumulation of strain along seismogenic faults in the shallower crust, it is difficult to evaluate this contribution to fault loading because it is unclear whether the viscous deformation occurs in localized shear zones or is more broadly distributed (Cowie et al. 2013). Nevertheless, viscosity and temperature have been applied to the model based on viscosity and heat versus depth diagrams from various studies related to the NW Iran and the world (e.g., Thatcher and Pollitz 2008; Watts et al. 2013; Earle 2015; Afshar et al. 2017; Shafaii Moghadam et al. 2018). For ease of operation and processing with minimal errors, we have applied the average heat and viscosity curves for each analytical layer. The upper crust, lower crust (~15–40 km) and upper mantle viscosities have been considered $1e26$ Pa s,

$1e20$ Pa s, and $1e18.5$ Pa s, respectively. In addition, the upper crust, lower crust, and upper mantle temperatures have been applied 200°, 700°, and 1100°, respectively.

The width of the NTF is reported to be about 20–25 km based on some studies (e.g. Ghanbari and Saedipoor 2015; Aghajany et al. 2017). The width of the other faults is chosen according to their length relative to the length of the largest fault in the study area (i.e. NTF). Therefore, the widths of the NBF, SBF, AF, AhF, and SF have been selected in 6.6, 10, 2.5, 6.5, and 2.2 km, respectively.

Taking the fault width into the model means defining the shear zone between fault blocks by connecting independent meshes with tie constraints. The internal friction angle of 30° is taken into account in the interaction of each shear zone.

The Young's modulus for the alluvial thin section, upper crust, lower crust, and upper mantle is considered 1 GPa, 50 GPa, 60 GPa, and 140 GPa, respectively.

The degree of freedom in the initial boundary conditions has been limited to the horizontal axis due to the control of loading conditions by GPS velocity vector data (Nazari et al. 2013) in this study. Boundary condition constraints have been removed due to the control of loading conditions by both GPS velocity vector data and static loading of the model topographic section in later stages of analysis. Rotational constraints have also been removed due to a combination of horizontal and vertical movements in the progressive stages of analysis.

Fault surfaces are defined according to their attitude from various references to the model (Table 4).

Therefore, the solid model had been completed by different nodal layers as well as boundary condition characters (Fig. 5).

6 Stress analysis

After completing and preparing the FE model described in the previous section, stress calculations are performed by loading. The results include stress outputs and energy diagrams.

The basis of stress calculations is the relationship between the reaction force and stress,

$$\frac{\partial}{\partial \mathrm{x}}\left(\mathrm{AE}\frac{\partial \mathrm{u}}{\partial \mathrm{x}}\right) = 0 \tag{12}$$

where E is the Young's modulus; u axial displacement; and A is the cross-section area. Interpolation model is based on the equations mentioned in Sect. 4. Here, variables include the displacement vector r(x,y,z). According to the mechanical condition of the model in a 3D mode, we can write the stress–strain relations using the Hooke's law,

$$\vec{\varepsilon} = \begin{Bmatrix} \varepsilon_{xx} \\ \varepsilon_{yy} \\ \varepsilon_{zz} \\ \varepsilon_{xy} \\ \varepsilon_{yz} \\ \varepsilon_{zx} \end{Bmatrix} = [\mathrm{C}]\vec{\sigma} + \overrightarrow{\varepsilon_0} \equiv [\mathrm{C}]\begin{Bmatrix} \sigma_{xx} \\ \sigma_{yy} \\ \sigma_{zz} \\ \sigma_{xy} \\ \sigma_{yz} \\ \sigma_{zx} \end{Bmatrix} + \begin{Bmatrix} \varepsilon_{xx0} \\ \varepsilon_{yy0} \\ \varepsilon_{zz0} \\ \varepsilon_{xy0} \\ \varepsilon_{yz0} \\ \varepsilon_{zx0} \end{Bmatrix} \tag{13}$$

where [C] is elastic coefficient matrix that is given by:

Table 4 The fault geometries used in the numerical model

Fault name	Segments	Length (km)	Strike	Dip	References
North Tabriz Fault (NTF)	North West	70	N120°	70°–90° NE	Ambraseys and Melville (1982), Berberian and Yeats (1999), Hessami et al. (2003), Karakhanian et al. (2004), Solaymani (2009), Rizza (2010), Fathian Baneh (2011), Ritz et al. (2011)
North Tabriz Fault (NTF)	South East	85	N120°	40°–60° NE	Ambraseys and Melville (1982), Berberian and Yeats (1999), Karakhanian et al. (2004), Solaymani (2009), Rizza (2010), Ritz et al. (2011)
North Bozghush Fault (NBF)	West/East	58 (43/15)	N106°/N055°	55°–70° N	Berberian and Yeats (1999), Seismotectonic atlas of Tabriz-Poldasht quadrangle, un-published
Sought Bozghush Fault (SBF)		78	N083°	50°–70° N	Berberian and Yeats (1999), Seismotectonic atlas of Tabriz-Poldasht quadrangle, un-published
Arasbaran Fault (AF)		20	N085°	75°–85° N	Nazari et al. (2013)
Ahar Fault (AhF)	Northwest/Central/Southeast	57 (9.5/28/18.8)	N104°	40°–50° NE	Solaymani (2009)
Sufian	West (Sharafkhaneh)/East	47 (29/18)	N085°	60°–80° NW	Berberian and Yeats (1999), Karakhanian et al. (2004), Ghahremani (2010)

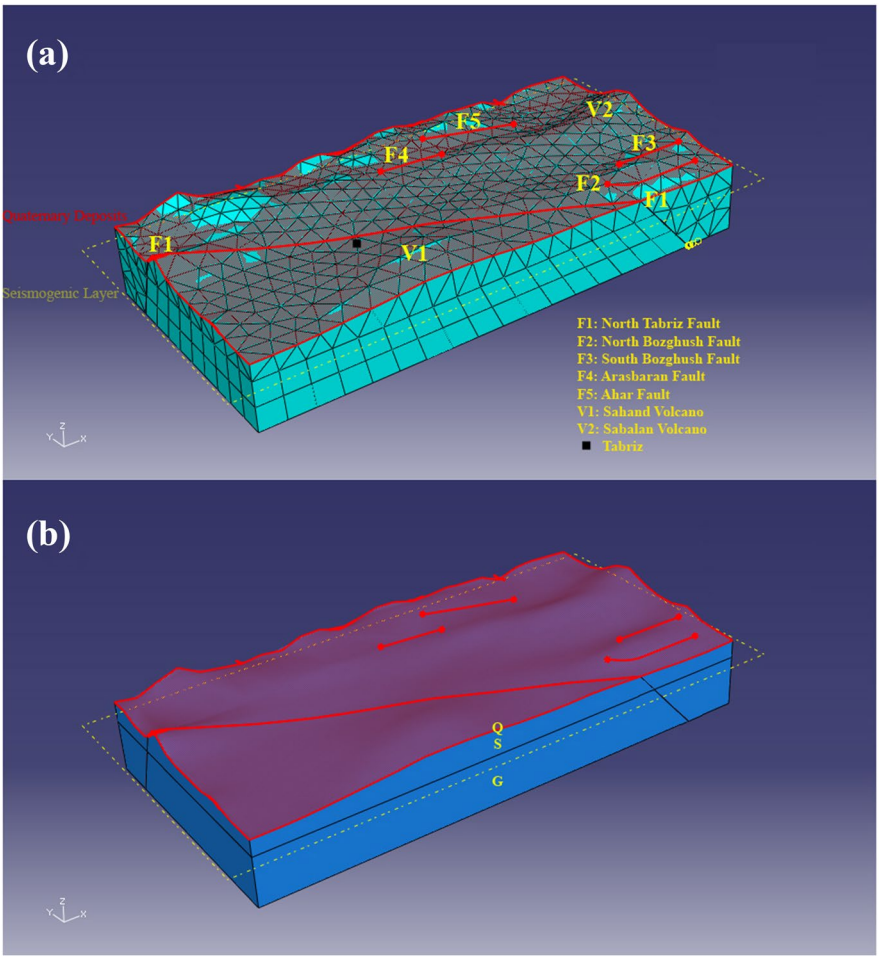

Fig. 5 Completed solid model by **a** boundary condition characters, **b** different nodal layers

$$[\mathrm{C}] = \frac{1}{\mathrm{E}}\begin{bmatrix} 1 & -\nu & -\nu & 0 & 0 & 0 \\ -\nu & 1 & -\nu & 0 & 0 & 0 \\ -\nu & -\nu & 1 & 0 & 0 & 0 \\ 0 & 0 & 0 & 2(1+\nu) & 0 & 0 \\ 0 & 0 & 0 & 0 & 2(1+\nu) & 0 \\ 0 & 0 & 0 & 0 & 0 & 2(1+\nu) \end{bmatrix} \tag{14}$$

where $\overrightarrow{\varepsilon_0}$ is internal strain vector and ν is Poisson's ratio.

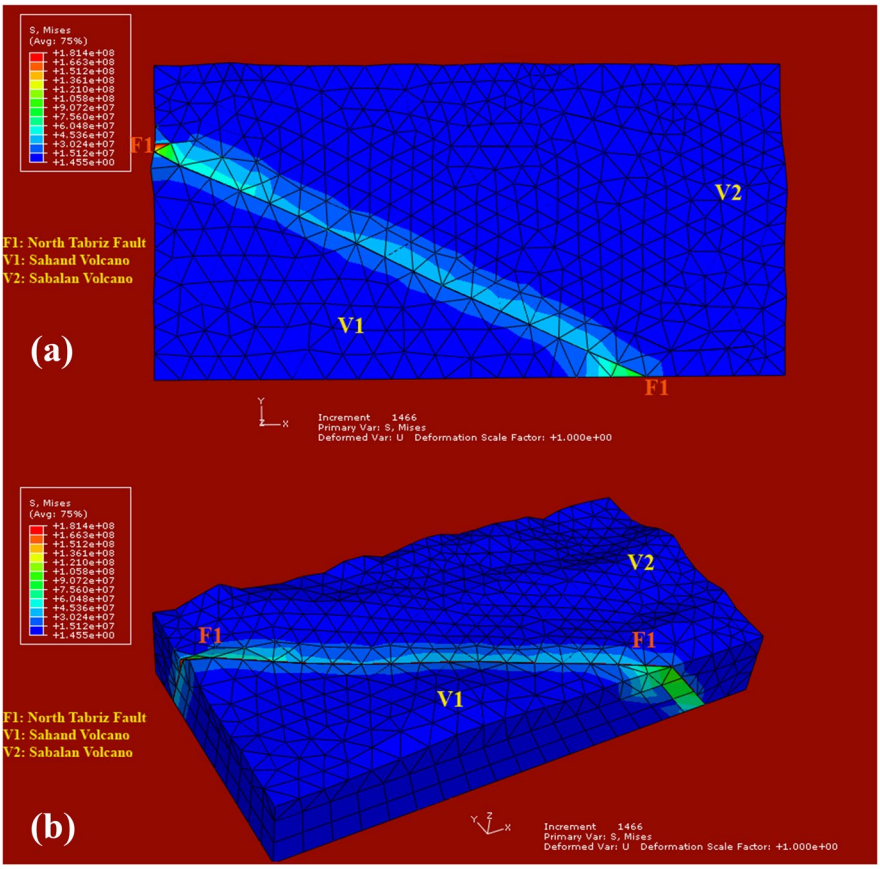

Fig. 6 **a** Stress accumulation zones in pre-failure mode. **b** 3D view of the stress accumulation zones in pre-failure mode along the NTF. The positive x-axis corresponds to east, and the positive y-axis represents to north

6.1 Stress outputs

Outputs are related to two pre-failure and failure modes. The pre-failure mode stress–strain response is normally expected to follow a linear elastic trend. The slope of the axial stress–axial strain curve for this trend yields the elastic modulus (Tutluoğlu et al. 2015).

We refer to the pre-failure mode in our finite element model where the rigidity of nodal connections on a fault plane reaches their weakest state. Theoretically, this mode is equivalent to the strain-hardening stage in the stress–strain curve. The pre-Failure mode is considered as a state in which the Mohr cycles are tangent to the Mohr–Coulomb failure envelope. In the pre-fracture mode, the blocks on both sides of the shear zone are locked to each other and the loading results in the accumulation of stress in the blocks. As the loading continues, the differential stresses will increase to the extent that new fractures occur. In the failure mode, the stress accumulation reaches its maximum level and that is the moment after which the two blocks will move towards each other immediately. In this study, we do not refer to the post-failure mode and complete release of stress, and therefore

consider the failure mode as the maximum stress in the stress–strain curve. Movement vectors in the failure mode are scattered on fault surfaces, but they are not epidemics and have not yet formed a single movement vector. Therefore, the stress accumulation on the output of the failure mode is related to episodic events.

Stress accumulations in the pre-failure mode are mainly around the North Tabriz Fault (NTF) and there are no stress accumulation evidences anywhere else in the study area (Fig. 6). Figure 7 represents a section of the model along the NTF to see and study depth changes of stress zones on the fault plane from different angles in pre-failure mode.

The second group of outputs is related to the stress behavior of model block in failure mode (Fig. 8). Figure 9 shows a section of the model along the NTF to see and study depth changes of stress zones on the fault plane from different angles in failure mode.

6.2 Energy outputs

Energy outputs include ALLIE, ALLKE, ETOTAL, and ALLVD diagrams that represent respectively the rate of internal, kinetic, total, and viscous dissipated energies per

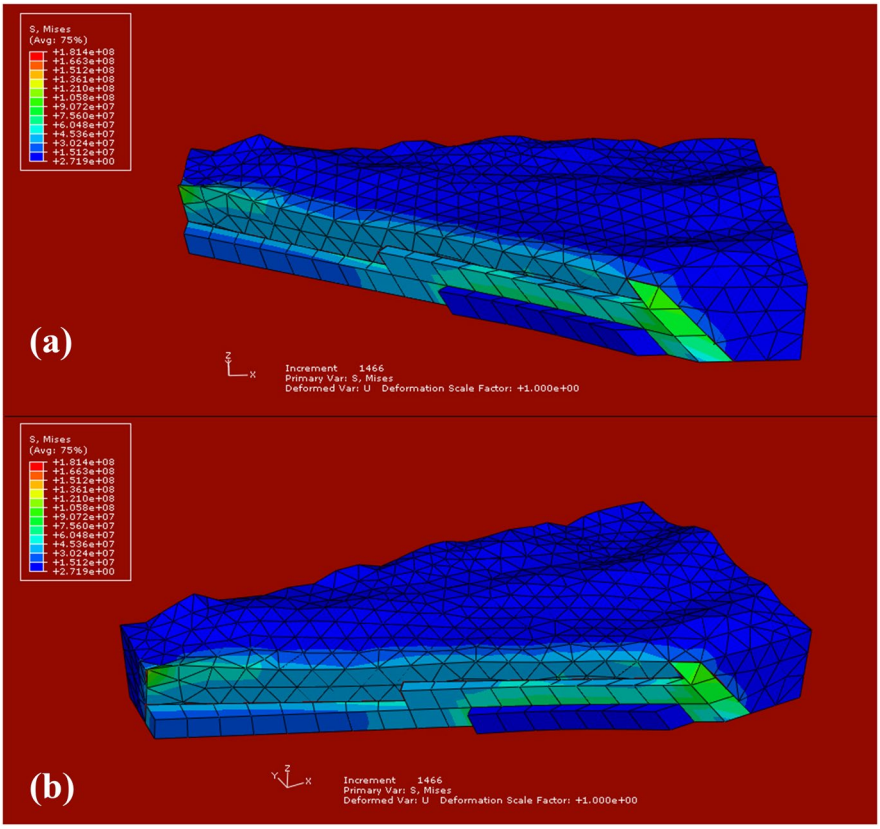

Fig. 7 **a** Stress accumulation zones on the NTF plane in pre-failure mode. **b** 3D view of the Stress accumulation zones on the NTF plane in pre-failure mode. The positive x-axis corresponds to east, and the positive y-axis represents to north

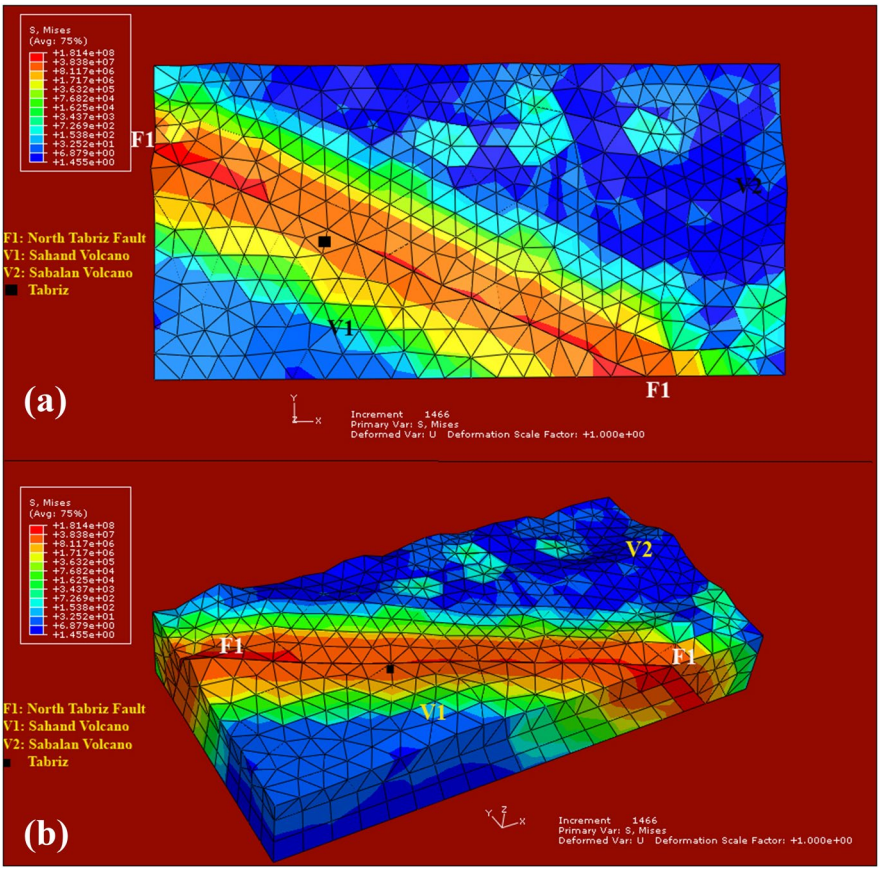

Fig. 8 **a** Stress accumulation zones on the NTF plane in failure mode. **b** 3D view of the stress accumulation zones for study area in failure mode. The positive x-axis corresponds to east, and the positive y-axis represents to north

time for the whole model (Fig. 10a–d). These outputs describe the energy changes in the time domain.

The total energy of an object is the constant sum of the potential and kinetic energies. The viscous dissipated energy is the energy dissipated by viscous effects. Deformation and flow of materials require energy. This mechanical energy is dissipated, i.e., during the flow it is converted into internal energy of the material (Winter 1987).

The ALLIE diagram for the entire model describes strictly ascending function that represents an increase of internal energy during the run time (Fig. 10a). ETOTAL diagram for the whole model describes a semi strictly ascending function showing an increase for total energy during the run time (Fig. 10b). However, the initial implementation stage is the time to see an energy drop during the initial run time. Subsequently, the ALLKE diagram for the whole model describes descending function that represents a decrease of kinetic energy during the run time (Fig. 10c). Similar to the previous diagram, the initial implementation stage is the time to see energy drop. Finally, the

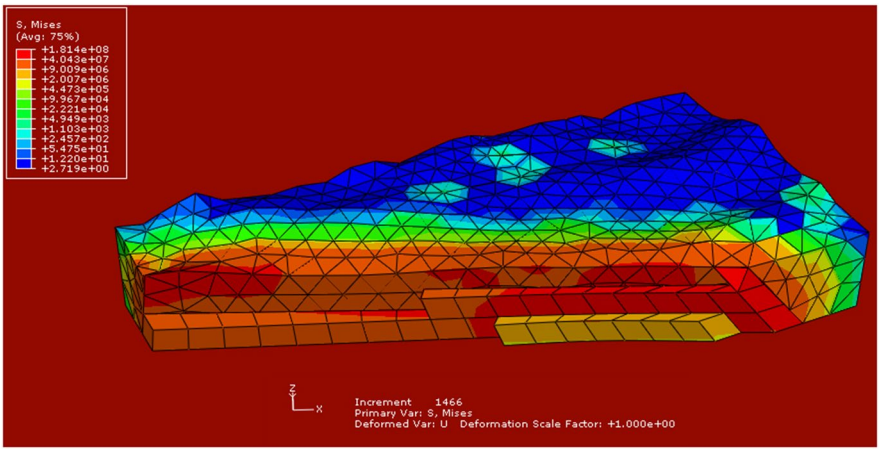

Fig. 9 Stress accumulation zones on the NTF plane in failure mode. The positive x-axis corresponds to east, and the positive z-axis represents to elevation

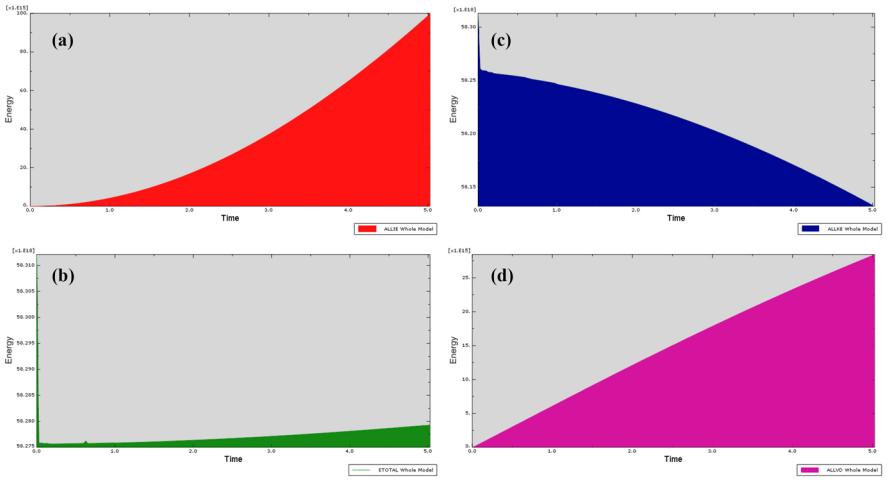

Fig. 10 Mechanical energy changes for the whole model. **a** ALLIE diagram representing the rate of internal energy per time, **b** ETOTAL diagram representing the rate of total energy per time **c** ALLKE diagram representing the rate of kinetic energy per time, and **d** ALLVD diagram representing the rate of viscous dissipated energy per time. The time axis is based on the number of months after first implementation

ALLVD diagram for the whole model describes ascending semi-linear function showing an increase in viscous dissipated energy during the run time (Fig. 10d).

7 Results and discussion

A validated solid model has analytical characteristics for our meshed topographic block. The FEA of the block diagram suggests the most stress bandwidth about 13 km in pre-failure mode. In this mode, stress accumulation is mainly around the NTF and there is no stress accumulation evidence anywhere else in the study area. In addition, northeast stress bandwidth along the fault strike is more than two times the southwest bandwidth of the fault line. Pre-failure mode-related stress accumulation anomalies in the southeast and northwest sectors of the NTF are mostly in the deeper and shallower areas, respectively. Most variations of the stress field are around the SBF in the upper layer of the crust that is made up of lighter rocks called SiAl. According to the Fig. 7b, the zone with highest stress accumulation appears in the shallow areas of the northwest sector of NTF. This stress accumulation seems to be influenced by the incremental topography in this sector of the fault. The most elongations of stress accumulation zones belong to the bottom of the SiAl zone in the central sector of the NTF, where Tabriz city is located next to it.

The results represent the high-stress accumulation zones around NTF in failure mode. However, the stress accumulation zones are evident in other locations of the research area. In these conditions, most stress bandwidth is about 60 km, which is three times the width of the NTF. The northeast stress bandwidth along the fault strike, at the same time, is almost equal to the southwest stress bandwidth along the fault line, but the northeast stress band has higher stress accumulation. In addition, maximum stress accumulation can be seen in the northwest, central, and southwest sectors of NTF respectively.

In other locations of research area, there are stress field anomalies around the tips of the main active faults. Some of these anomalies include stress accumulation zones related to the AF, AhF, and SBF.

A notable issue with this output is the high average stress accumulation in the southeast block of the NTF relative to the northeast block. Since incipient failure and instability is due to the differential stress and Mohr's circle touching the Mohr–Coulomb failure surface, unlike the northeast block, the southwest block is expected to have more stability because tolerate more differential stress. Based on output results of stress analysis stress accumulation zones have most anomalies and high differential stress in depth areas of the southeast sector of NTF so that most anomalies are zones close to the SBF in SiAl zone. In addition, the zones with highest stress accumulation appear in the shallow areas at the end of the northwest sector of NTF (Fig. 9). This stress accumulation seems to be influenced by the incremental topography in this sector of the fault. The most elongations of stress accumulation zones belong to the bottom of the SiAl zone in the central sector of the NTF.

The ALLIE diagram gives us an insight into the internal strain energy. The internal strain energy is equal to the area under the stress–strain curve in both pre-failure and failure modes. The linearity of the stress–strain graph at the elastic behavior stage indicates the constant stress–strain ratio. In this analysis, the strictly ascending ALLIE function suggests the nonlinearity of the stress–strain graph in the elastic behavior stage. Therefore, during the loading time, the stress–strain ratio is constantly increasing. This means that after each seismic event, more stress is required to deform the fault block elements and to achieve the next seismic event. The energy drop at the beginning of the run time in the ETOTAL

diagram indicates the locking of the elements as a result of the collision of the shear zone blocks, resulting in an energy drop in the ALLKE and subsequently a total energy drop. In addition, the decrease in ALLKE during run time is the main cause of the low slope of the ETOTAL diagram.

The mechanical energy required for the deformation and flow of the rock materials is dissipated during the flow and converted to the internal energy of the rock material. Therefore, the ascending ALLVD function represents the conversion of ALLVD to ALLIE during the run time. By defining an appropriate time scale to the analytical model, the pattern of these four diagrams together can be a model to guide us in recognizing the time of maximum stress accumulation and an impending event.

8 Conclusions

Stress accumulation results in pre-failure mode represent that stress accumulation is mainly around the NTF and there is no stress accumulation evidence anywhere else in the study area. In addition, northeast stress bandwidth along the NTF strike is more than two times the southwest bandwidth along the fault line. Stress accumulations related to both pre-failure and failure modes have more anomalies in the deeper and shallow areas of the southeast and northwest sectors respectively in the NTF. The most elongations of stress accumulation zones in both pre-failure and failure modes belong to the bottom of the SiAl zone in the central sector of the NTF. The outputs of failure mode suggest that stress accumulation zones are evident to the tips of the main active faults. Energy diagrams, based on the total energy consumed in the form of internal strain energy, show a nonlinear increase in the stress–strain ratio in the progressive stages of analysis. The pattern of stress accumulation distribution along with the hybrid model of energy diagrams can provide insight into the location and timing of earthquakes and events, if accompanied by a suitable time scale. This study is a preliminary numerical analysis of the three-dimensional model and has many shortcomings. This modeling can be an approach for understanding the physical behavior of the Earth at different time scales. Subsequent work will include a more detailed definition of model rheology at different layers, advanced boundary conditions, considering the underside topography of the model layers, and the definition of a suitable time scale over a specified interval.

Acknowledgements We thank General Governor Office and Department of Roads and Urban Development of East Azerbaijan who shared their information and knowledge about topography data.

References

Abd-Elmotaal H (2013) Behaviour of earth's crust due to topographic loads derived by inverse and direct isostasy. NRIAG J Astron Geophys 2:196–202. https://doi.org/10.1016/j.nrjag.2013.12.005

Afshar A, Norouzi GH, Moradzadeh A, Riahi MA, Porkhial S (2017) Curie point depth, geothermal gradient and heat-flow estimation and geothermal anomaly exploration from integrated analysis of aeromagnetic and gravity data on the Sabalan Area, NW Iran. Pure Appl Geophys 174:1133–1152. https://doi.org/10.1007/s00024-016-1448-z

Aghajany SH, Voosoghi B, Yazdian A (2017) Estimation of north Tabriz fault parameters using neural networks and 3D tropospherically corrected surface displacement field. Geomat Nat Hazards Risk 8:918–932. https://doi.org/10.1080/19475705.2017.1289248

Allik H, Hughes TJR (1970) Finite element method for piezoelectric vibration. Int J Numer Methods Eng 2:151–157. https://doi.org/10.1002/nme.1620020202

Ambraseys N, Melville C (1982) A History of Persian Earthquakes. Cambridge University Press, Cambridge
Amadei B, Stephansson O (1997) Rock stress and its measurement. Chapman and Hall, London
Bai Y, Xu X (2013) Apply of explicit finite element in seismic ground motion computation. JAMP 1:11–14. https://doi.org/10.4236/jamp.2013.16003
Berberian M, Yeats RS (1999) Patterns of historical earthquake rupture in the Iranian Plateau. B Seismol Soc Am 89:120–139
Billings SD, Sambridge MS, Kennett BLN (1994) Errors in hypocenter location: picking, model, and magnitude dependence. Bull Seism Soc Am 84:1978–1990
Boissonnat JD (1988) Shape reconstruction from planar cross sections. Comput Vision Graph 44:1–29. https://doi.org/10.1016/S0734-189X(88)80028-8
Bombolakis EG (1989) Thrust fault mechanics and dynamics during a developmental stage of a foreland belt. J Struct Geol 11:439–455. https://doi.org/10.1016/0191-8141(89)90021-7
Caendish JC, Field DA, Frey WH (1985) An approach to automatic three-dimensional finite element mesh generation. Int J Numer Methods Eng 21:329–347. https://doi.org/10.1002/nme.1620210210
Carminati E, Vadacca L (2010) Two- and three-dimensional numerical simulations of the stress field at the thrust front of the Northern Apennines, Italy. J Geophys Res 115:B12425. https://doi.org/10.1029/2010JB007870
Carminati E, Toniolo Augier F, Barba S (2001) Dynamic modelling of stress accumulation in Central Italy: role of structural heterogeneities and rheology. Geophys J Int 144:373–390. https://doi.org/10.1046/j.1365-246x.2001.00323.x
Chen T, Wang X, Mukerji T (2014) Evaluation of stress concentration in a coal mine panel using seismic data. In: Sun S, Wang S (eds) An interdisciplinary response to mine water challenges. China University of Mining and Technology Press, Xuzhou, pp 269–272
Chéry J, Zoback MD, Hassani R (2001) An integrated mechanical model of the San Andreas fault in central and northern California. J Geophys Res 106:22051–22066. https://doi.org/10.1029/2001JB000382
Chéry J, Zoback MD, Hickman S (2004) A mechanical model of the San Andreas fault and SAFOD pilot hole stress measurements. Geophys Res Lett 31:1–5. https://doi.org/10.1029/2004GL019521
Cowie PA, Scholz CH, Roberts GP, Walker JF, Steer P (2013) Viscous roots of active seismogenic faults revealed by geologic slip rate variations. Nat Geosci 6:1036. https://doi.org/10.1038/ngeo1991
Dal Zilio L, van Dinther Y, Gerya TV, Pranger CC (2018) Seismic behaviour of mountain belts controlled by plate convergence rate. Earth Planet Sci Lett 482:81–92. https://doi.org/10.1016/j.epsl.2017.10.053
Davis JC (1986) Statistics and Data Analysis in Geology. John Wiley & Sons, New York
Debnath SK, Sen S (2013) Pattern of stress-strain accumulation due to a long dip slip fault movement in a viscoelastic layered model of the lithosphere–Asthenosphere system. Int J Appl Mech Eng 18:653–670. https://doi.org/10.2478/ijame-2013-0040
Deng J, Sykes LR (1997) Evolution of the stress field in southern California and triggering of moderate-size earthquakes: a 200-year perspective. J Geophys Res 102:9859–9886. https://doi.org/10.1029/96JB03897
Earle S (2015) Physical geology. BCCampus Open Textbook Project. https://opentextbc.ca/geology/
Fathian Baneh A (2011) Paleoseismological investigations along the North Tabriz Fault. MSc thesis, Islamic Azad University. [**in Persian**]
Freed AM, Ali ST, Bürgmann R (2007) Evolution of stress in southern California for the past 200 years from coseismic, postseismic and interseismic stress changes. Geophys J Int 169:1164–1179. https://doi.org/10.1111/j.1365-246X.2007.03391.x
Fuis SG, Scheirer SD, Langenheim EV, Kohler DM (2012) A new perspective on the geometry of the San Andreas fault of South California and relationship to lithospheric structure. Bull Seismol Soc Am 102:1236–1251. https://doi.org/10.1785/0120110041
Garimella RV (2002) Mesh data structure selection for mesh generation and FEA applications. Int J Numer Methods Eng 55:451–478. https://doi.org/10.1002/nme.509
Ghanbari E, Saedipoor K (2015) Paleo and new earthquakes and evaluation of North Tabriz fault displacement in relation to recurrence interval of destructive earthquakes. J Civ Eng Archit 9:1012–1016. https://doi.org/10.17265/1934-7359/2015.08.013
Ghahremani A (2010) Morphotectonic investigations along the Shabestar Fault. MSc thesis, Islamic Azad University. [**in Persian**]
Günther T, Rücker C (2005) A triple-grid technique for the 3d inversion of dc resistivity data incorporating arbitrary topography. In: 19th Annual symposium on the application of geophysics to engineering and environmental problems (Abstract), Palermo, 5–8 Sept, p 4

Herrin E, Negraru P, Golden P, Mulcahy C (2002) Local site effects at the Nevada Seismic Array (NVAR). In: Proceedings of the 24th seismic research symposium, technologies for monitoring the comprehensive nuclear-test-ban treaty, Florida, 17–19 Sept, pp 340–349

Hessami K, Jamali F, Tabassi H (2003) Major active faults of Iran. International Institute of Earthquake Engineering and Seismology, scale 1:250,000.

Karakhanian AS, Trifonov VG, Philip H, Avagyan A, Hessami K, Jamali F, Bayraktutan MS, Bagdassarian H, Arakelian S, Davtian V, Adilkhanyan A (2004) Active faulting and natural hazards in Armenia, eastern Turkey and northwestern Iran. Tectonophysics 380:189–219. https://doi.org/10.1016/j.tecto.2003.09.020

Lysmer J, Drake LA (1972) A finite element method for seismology. In: Fernbach S, Bolt BA (eds) Alder B. Methods in computational physics, New York, pp 181–216

Mandl G (2000) Faulting in brittle rocks: an introduction to the mechanics of tectonic faults. Springer, Berlin

Mareschal JC, Kuang J (1986) Intraplate stresses and seismicity: the role of topography and density heterogeneities. Tectonophysics 132:153–162. https://doi.org/10.1016/0040-1951(86)90030-2

Mignan A, Bowman DD, King GCP (2006) An observational test of the origin of accelerating moment release before large earthquakes. J Geophys Res 111:1–14. https://doi.org/10.1029/2006JB004374

Nalbant SS, Mccloskey J, Steacy S, Barka AA (2002) Stress accumulation and increased seismic risk in eastern Turkey. Earth Planet Sci Lett 195:291–298. https://doi.org/10.1016/S0012-821X(01)00592-1

Nazari H, Talebian M, Ghorashi M (2013) Seismotectonic map of NW Iran (1:750,000). Geological Survey, Iran

Nelson RA (1985) Geologic analysis of naturally fractured reservoirs. Gulf Publishing, Houston

Niño F, Chéry J, Gratier JP (1998) Mechanical modeling of compressional basins: origin and interaction of faults, erosion, and subsidence in the Ventura basin, California. Tectonics 17:955–972. https://doi.org/10.1029/1998TC900007

Pain CC, Herwanger JV, Worthington MH, De Oliveira CRE (2002) Effective multidimensional resistivity inversion using finite-element techniques. Geophys J Int 151:710–728. https://doi.org/10.1046/j.1365-246X.2002.01786.x

Pereyra V, Richardson E, Zarantonello SE (1992) Large scale calculations of 3D elastic wave propagation in a complex geology. In: Proceedings of the 1992 ACM/IEEE conference on supercomputing, Supercomputing'92, Minneapolis, 16–20 Nov, pp 301-309

Pollard DD (2000) Strain and stress: discussion. J Struct Geol 22:1359–1367. https://doi.org/10.1016/S0191-8141(00)00047-X

Pollitz F, Bakun WH, Nyst M (2004) A physical model for strain accumulation in the San Francisco Bay region: stress evolution since 1838. J Geophys Res 109:1–16. https://doi.org/10.1029/2004JB003003

Rao SS (2011) The finite element method in engineering, 5th edn. Elsevier Butterworth Heinemann, Boston

Rhoden AR, Wurman G, Huff EM, Manga M, Hurford TA (2012) Shell tectonics: a mechanical model for strike-slip displacement on Europa. Icarus 218:297–307. https://doi.org/10.1016/j.icarus.2011.12.015

Ritz JR, Rizza M, Vernant P, Peyret M, Nazari H, Nankali H, Djamour Y, Mahan S, Salamati R, Tavakoli F (2011) Morphotectonics and geodetic evidences for a constant slip–rate along the Tabriz Fault (Iran) during the past 45 kyr. Geophys J Int 193:1083–1094. https://doi.org/10.1093/gji/ggt041

Rizza M (2010) Analyses des vitesses et des déplacements cosismiques sur des failles décrochantes en Mongolie et en Iran: approche morphotectonique et paléosismologique: PhD thesis, University of Montpellier 2. [**in French**]

Ryder I, Bürgmann R, Fielding E (2012) Static stress interactions in extensional earthquake sequences: an example from the South Lunggar Rift, Tibet. J Geophys Res 117:1–18. https://doi.org/10.1029/2012JB009365

Sadeghi-Farshbaf P (2010) Governor model and mechanism to the structural strikes and trends for eastern region of Taftan volcano, Iran. MSc thesis, University of Sistan & Baluchestan (in Persian)

Sadeghi-Farshbaf P (2016) Identifying zones with high stress accumulation around the active faults by three-dimensional simulations based on finite elements: a case study of the East Azerbaijan, Iran. PhD thesis, University of Birjand (in Persian)

Sadeghi-Farshbaf P, Khatib MM, Moridi AA, Bagheri S (2015) 3D mechanical modeling of faults planes based on stress fields: a case study of Saravan fault, SE Iran. Model Earth Syst Environ 1:1–11. https://doi.org/10.1007/s40808-015-0046-x

Sadeghi-Farshbaf P, Khatib MM, Nazari H (2015) Solid meshing of 3D geological model in finite element analysis: a case study of East Azerbaijan, NW Iran. Model Earth Syst Environ 2:1–7. https://doi.org/10.1007/s40808-015-0066-6

Sambridge M, Braun J, McQueen H (1995) Geophysical parametrization and interpolation of irregular data using natural neighbours. Geophys J Int 122:837–857. https://doi.org/10.1111/j.1365-246X.1995.tb06841.x

Shafaii Moghadam H, Griffin WL, Kirchenbaur M, Garbe-Schönberg D, Zakie Khedr M, Kimura JI, Stern RJ, Ghorbani G, Murphy R, O'Reilly SY, Arai S (2018) Roll-back, extension and mantle upwelling triggered eocene potassic magmatism in NW Iran. J Petrol 59:1417–1465. https://doi.org/10.1093/petrology/egy067

Shao B, Hou G (2019) The interactions of fault patterns and stress fields during active faulting in Central North China Block: insights from numerical simulations. PLoS ONE 14:e0215893. https://doi.org/10.1371/journal.pone.0215893

Smith B, Sandwell D (2003) Coulomb stress accumulation along the San Andreas Fault system. J Geophys Res 108:1–17. https://doi.org/10.1029/2002JB002136

Solaymani S (2009) Evaluation de l'aléa sismique pour les villes de Téhéran, Tabriz et Zandjan dans le NW de l'Iran. Approche morphotectonique et paléosismologique. PhD thesis, University of Montpellier 2. [**in French**]

Talwani P (1990) Neotectonics in the southeastern United States with emphasis on the Charleston, South Carolina, area. In: Krinitzsky EL, Slemmons DB (eds) Neotectonics in earthquake evaluation. Geological Society of America, Colorado, pp 11–129

Teknik V, Ghods A (2017) Depth of magnetic basement in Iran based on fractal spectral analysis of aeromagnetic data. Geophys J Int 209:1878–1891. https://doi.org/10.1093/gji/ggx132

Thatcher W, Pollitz FF (2008) Temporal evolution of continental lithospheric strength in actively deforming regions. GSA Today 18:4. https://doi.org/10.1130/GSAT01804-5A.1

Turcotte DL (1977) Stress accumulation and release on the San Andreas Fault. Pure Appl Geophys 115:413–427. https://doi.org/10.1007/BF01637118

Tutluoğlu L, Öge İF, Karpuz C (2015) Relationship between pre-failure and post-failure mechanical properties of rock material of different origin. Rock Mech Rock Eng 48:121–141. https://doi.org/10.1007/s00603-014-0549-1

Vasheghani-Farahani J, Zaré M (2014) Seismological aspects of the Varzeghan twin Earthquakes on 11 August 2012 (Mw 6.3 and Mw 6.1), in East Azerbaijan province, NW Iran. Episodes 37:96–104

Watts AB, Zhong SJ, Hunter J (2013) The behavior of the lithosphere on seismic to geologic timescales. Annu Rev Earth Planet Sci 41:443–468. https://doi.org/10.1146/annurev-earth-042711-105457

Winter HH (1987) Viscous dissipation term in energy equations. American Institute of Chemical Engineers Modular Instruction 7:261–268

Xiao J, He J (2015) 3D Finite-Element Modeling of Earthquake Interaction and Stress Accumulation on Main Active Faults around the Northeastern Tibetan Plateau Edge in the Past ~100 Years. B Seismol Soc Am 105:1–12. https://doi.org/10.1785/0120140342

Xing H, Yu W, Zhang J (2009) 3D mesh generation in geocomputing. Lect Notes Earth Sci 119:27–64. https://doi.org/10.1007/978-3-540-85879-9_2